# Piezoelectric Nanocavity Interface for Strong Coupling between a Superconducting Circuit, Phonon, and Spin

Hamza Raniwala[1], Stefan Krastanov,[1] Lisa Hackett,[2] Matt Eichenfield,[2] Dirk R. Englund,[1,3] and Matthew E. Trusheim[1,4,*]

[1]*Department of Electrical Engineering and Computer Science, Massachusetts Institute of Technology, Cambridge, Massachusetts 02139, USA*
[2]*Sandia National Laboratories, Albuqurque, New Mexico, USA*
[3]*Research Laboratory of Electronics, Massachusetts Institute of Technology, Cambridge, Massachusetts 02139, USA*
[4]*DEVCOM, Army Research Laboratory, Adelphi, Maryland 20783, USA*

We introduce a hybrid tripartite quantum system for strong coupling between a semiconductor spin, a mechanical phonon, and a microwave excitation of a superconducting circuit. Consisting of a piezoelectric resonator with an integrated diamond strain concentrator, this system achieves microwave-acoustic and spin-acoustic coupling rates of approximately megahertz or greater, allowing simultaneous ultrahigh cooperativities (approximately $10^3$ and approximately $10^2$, respectively). From finite-element modeling and master-equation simulations, we estimate superconducting-circuit-to-spin quantum state transfer fidelities exceeding 0.95 on the basis of separately demonstrated device parameters. We anticipate that this device will enable hybrid quantum architectures that leverage the advantages of both superconducting circuits and solid-state spins for information processing, memory, and networking.

## I. INTRODUCTION

Solid-state quantum systems based on superconductors and spins are leading platforms that offer complementary advantages in quantum computing and networking. Superconducting quantum processors enable fast and high-fidelity entangling gates [1,2], but challenges remain in quantum memory time and long-distance networking. Conversely, atomlike emitters in the solid state have demonstrated long spin coherence times, efficient spin-photon interfaces for long-distance entanglement, and high readout fidelity [3–8]. Coupling these modalities is therefore an exciting direction in quantum information science.

Studies using magnetic coupling between microwave (MW) photons and spins have been limited to multispin ensemble interactions [9–15] due to low spin magnetic susceptibility and the low magnetic energy density of MW resonators [16–18]. Alternative experiments and proposals rely on coupling via intermediate acoustic modes [19–21], which have experimentally demonstrated large coupling to superconducting circuits (SCs) [22–28] and are predicted to have large coupling to diamond quantum emitters [29–35], or low-frequency mechanical driving of quantum emitters [36,37]. However, designing a device that strongly couples one phonon to both one MW photon and one spin—enabling an efficient MW-photon-to-spin interface—remains an outstanding challenge.

Here we address this prolem through the codesign of a scandium-doped aluminum nitride ($Sc_{0.32}Al_{0.68}N$) Lamb-wave resonator with a heterogeneously integrated diamond thin film. This structure piezoelectrically couples a MW photon and an acoustic phonon, while concentrating strain at the location of a diamond quantum emitter. Through finite-element modeling, we predict photon-phonon coupling of approximately 10 MHz concurrent with phonon-spin coupling of approximately 3 MHz. These rates yield photon-phonon and phonon-spin cooperativities on the order of $10^4$ assuming demonstrated lifetimes of spins, mechanical resonators, and superconducting circuits [38,39]. We explore state-transfer protocols via quantum master equation simulations, and show that this device can achieve photon-to-spin transduction fidelity $F > 0.97$ with conservative hardware parameters. We find that the performance of these schemes is likely limited by two-level-system (TLS) loss in current piezoelectrics. A reduction in piezoelectric TLS loss rates to that of silicon will pave the way toward SC-state–spin-state transduction with $F > 0.99$.

*mtrush@mit.edu

## II. THEORY OF MW-PHOTON–PHONON AND PHONON-SPIN COUPLING

We consider a coupled tripartite system consisting of a SC, acoustic phonon, and group-IV electron spin (see Fig. 1).

First, we review the transmon architecture, which consists of a superconducting quantum interference device loop with combined Josephson energy $E_J$ and capacitance $C_J$ in parallel with a shunt capacitor $C_S$. For the sake of constructing only the coupled system, we omit the transmon readout resonator, which typically consists of a quarter-wave resonator coupled in parallel to the transmon. The transmon's Josephson and charging energies are given by $E_J(\phi) = (I_C \Phi_0/\pi) \cos(\phi_{\text{ext}}) = E_J \cos(\phi_{\text{ext}})$ and $E_C = e^2/2(C_S + C_J)$ ($I_C$ is the Josephson-junction critical current). Note here that the total charging energy for $\hat{n}$ Cooper pairs is $4E_C\hat{n}$, where $\hat{\phi}$ is the conjugate variable of $\hat{n}$. Then the transmon Hamiltonian is given by

$$\hat{H}_{\text{transmon}} = 4E_C\hat{n} + E_J(\hat{\phi}) \tag{1}$$

$$= 4E_C\hat{n} + E_J \left( \hat{\phi} + \frac{1}{2}\hat{\phi}^2 + \frac{1}{6}\hat{\phi}^3 + \frac{1}{12}\hat{\phi}^4 + \cdots \right) \tag{2}$$

$$\approx \left( \sqrt{8E_J E_C} - E_C \right) \hat{a}^\dagger \hat{a} - E_C(\hat{a}^\dagger \hat{a}^\dagger \hat{a} \hat{a}). \tag{3}$$

In the last step, we have rewritten the expression in terms of the ladder operators. If we approximate the transmon as a two-level system, then we can simply write $\hat{H}_{\text{transmon}}$ as

$$\hat{H}_{\text{transmon}}/\hbar = \frac{\omega_{\text{SC}}}{2}\hat{\sigma}^z_{\text{SC}}. \tag{4}$$

Next, we give the Hamiltonian of the electromechanical resonator. Without coupling, the resonator modes can each be approximated as harmonic oscillators with energy $\hbar\omega_{p,k}$, where $\omega_{p,k}$ is the resonant frequency of the $k$th resonator mode, plus some vacuum-energy terms. Ignoring these terms, we find the Hamiltonian $H_{\text{res}}$ is given by

$$\hat{H}_{\text{res}}/\hbar = \sum_k \omega_{p,k}\hat{a}^\dagger_{p,k}\hat{a}_{p,k}. \tag{5}$$

Finally, we consider the Hamiltonian of the group-IV electron spin. The full Hamiltonian of group-IV color centers is discussed at length in Ref. [40], but for the purposes of this paper, we consider the system under an off-axis (transverse and longitudinal) magnetic field (discussed in Ref. [20]). In these conditions, the group-IV Hamiltonian can be written as the sum of the spin-orbit Hamiltonian $\hat{H}^{\text{SO}}$ and a Zeeman perturbation $\hat{H}^Z$ (in the $\{|e_x \uparrow\rangle, |e_y \uparrow\rangle, |e_x \downarrow\rangle, |e_y \downarrow\rangle\}$ basis),

$$\hat{H}_{\text{spin}} = \hat{H}^{\text{SO}} + \hat{H}^Z \tag{6}$$

$$= \begin{bmatrix} 0 & 0 & -i\lambda_g & 0 \\ 0 & 0 & 0 & i\lambda_g \\ i\lambda_g & 0 & 0 & 0 \\ 0 & -i\lambda_g & 0 & 0 \end{bmatrix}$$

$$+ \begin{bmatrix} \gamma_s B_z & \gamma_s B_x & iq\gamma_L B_z & 0 \\ \gamma_s B_x & -\gamma_s B_z & 0 & -iq\gamma_L B_z \\ -iq\gamma_L B_z & 0 & \gamma_s B_z & \gamma_s B_x \\ 0 & iq\gamma_L B_z & \gamma_s B_x & -\gamma_s B_z \end{bmatrix} \tag{7}$$

$$= \begin{bmatrix} \gamma_s B_z & \gamma_s B_x & -i\lambda & 0 \\ \gamma_s B_x & -\gamma_s B_z & 0 & i\lambda \\ i\lambda & 0 & \gamma_s B_z & \gamma_s B_x \\ 0 & -i\lambda & \gamma_s B_x & -\gamma_s B_z \end{bmatrix}, \tag{8}$$

where we use $\lambda \equiv \lambda_g - q\gamma_L B_z$ [40]. Solving the eigensystem of this Hamiltonian gives us the eigenvalues

$$\nu_1 = -\sqrt{\gamma_s^2 B_x^2 + (\lambda_-)^2}, \tag{9}$$

$$\nu_2 = \sqrt{\gamma_s^2 B_x^2 + (\lambda_-)^2}, \tag{10}$$

$$\nu_3 = -\sqrt{\gamma_s^2 B_x^2 + (\lambda_+)^2}, \tag{11}$$

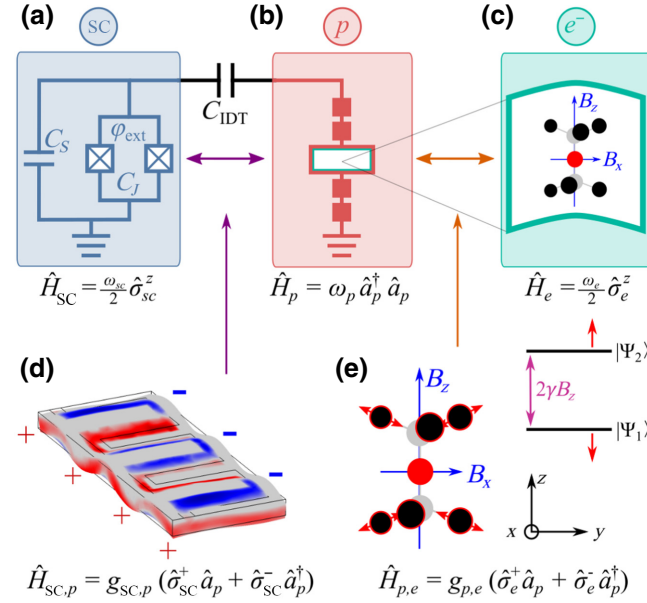$$\nu_4 = \sqrt{\gamma_s^2 B_x^2 + (\lambda_+)^2} \tag{12}$$



FIG. 1. Coupled SC-phonon-spin quantum system. (a)–(c) The uncoupled modes of the (a) superconducting qubit with Josephson capacitance $C_J$, shunt capacitance $C_S$, and external flux bias $\phi_{\text{ext}}$; (b) acoustic mode capacitively coupled by $C_{\text{IDT}}$; and (c) diamond quantum emitter. (d) Piezoelectric interaction, where the color indicates the electric field profile under mechanical displacement. (e) Spin-strain coupling resulting from modulation of the interatomic distance of the quantum emitter via mechanical strain under an external magnetic field $\mathbf{B} = B_x\hat{\mathbf{x}} + B_z\hat{\mathbf{z}}$ with spin gyromagnetic ratio $\gamma$.

$$\hat{H}_{\text{SC}} = \frac{\omega_{sc}}{2}\hat{\sigma}^z_{sc} \quad \hat{H}_p = \omega_p \hat{a}^\dagger_p \hat{a}_p \quad \hat{H}_e = \frac{\omega_e}{2}\hat{\sigma}^z_e$$

$$\hat{H}_{\text{SC},p} = g_{\text{SC},p} (\hat{\sigma}^+_{\text{SC}} \hat{a}_p + \hat{\sigma}^-_{\text{SC}} \hat{a}^\dagger_p) \quad \hat{H}_{p,e} = g_{p,e} (\hat{\sigma}^+_e \hat{a}_p + \hat{\sigma}^-_e \hat{a}^\dagger_p)$$

and the associated eigenvectors

$$|\psi_1\rangle = \left(\frac{1}{2\sqrt{\gamma_s^2 B_x^2 - (\lambda_-)(\lambda_- + \nu_2)}}\right)[(-i(\lambda_- + \nu_2))|e_x \uparrow\rangle + i|e_x \downarrow\rangle - (\lambda_- + \nu_2)|e_y \uparrow\rangle + |e_y \downarrow\rangle], \qquad (13)$$

$$|\psi_2\rangle = \left(\frac{1}{2\sqrt{\gamma_s^2 B_x^2 + (\lambda_-)(\lambda_- + \nu_2)}}\right)\left[-i\left(\frac{\lambda_- + \nu_1}{\lambda_- + \nu_2}\right)|e_x \uparrow\rangle + i|e_x \downarrow\rangle - \left(\frac{\lambda_- + \nu_1}{\lambda_- + \nu_2}\right)|e_y \uparrow\rangle + |e_y \downarrow\rangle\right], \qquad (14)$$

$$|\psi_3\rangle = \left(\frac{1}{2\sqrt{\gamma_s^2 B_x^2 + (\lambda_+)(\lambda_+ + \nu_4)}}\right)\left[-i\left(\frac{\lambda_+ + \nu_3}{\lambda_+ + \nu_4}\right)|e_x \uparrow\rangle + i|e_x \downarrow\rangle - \left(\frac{\lambda_+ + \nu_3}{\lambda_+ + \nu_4}\right)|e_y \uparrow\rangle + |e_y \downarrow\rangle\right], \qquad (15)$$

$$|\psi_4\rangle = \left(\frac{1}{2\sqrt{\gamma_s^2 B_x^2 + (\lambda_+)(\lambda_+ + \nu_4)}}\right)[(-i(\lambda_+ + \nu_4))|e_x \uparrow\rangle - i|e_x \downarrow\rangle + (\lambda_+ + \nu_4)|e_y \uparrow\rangle + |e_y \downarrow\rangle], \qquad (16)$$

where we use $\lambda_- = \lambda - \gamma_s B_z$ and $\lambda_+ = \lambda + \gamma_s B_z$. (Note that in the limit where $B_x \to 0$, these eigenvectors and eigenvalues simplify as $\{|\psi_1\rangle, |\psi_2\rangle, |\psi_3\rangle, |\psi_4\rangle\} \to \{|e_+ \uparrow\rangle, |e_+ \downarrow\rangle, |e_- \downarrow\rangle, |e_- \uparrow\rangle\}$ from Ref. [40].)

Finally, the rate of coupling $g_{p,e}$ between the lowest-lying states $|\psi_1\rangle$ and $|\psi_3\rangle$ can be calculated as

$$\frac{g_{p,e}}{2\pi} = \left|\langle\psi_3|M^{-1}H_{\text{strain}}M|\psi_1\rangle\right|, \qquad (17)$$

where

$$H_{\text{strain}} = \begin{bmatrix} \alpha & 0 & \beta & 0 \\ 0 & \alpha & 0 & \beta \\ \beta & 0 & -\alpha & 0 \\ 0 & \beta & 0 & -\alpha \end{bmatrix} \qquad (18)$$

and $M$ is the matrix that transforms the eigenvectors $\psi_i$ to the strain basis, such that

$$M\hat{H}_{\text{spin}} = M \begin{bmatrix} \nu_1 & 0 & 0 & 0 \\ 0 & \nu_2 & 0 & 0 \\ 0 & 0 & \nu_3 & 0 \\ 0 & 0 & 0 & \nu_4 \end{bmatrix}. \qquad (19)$$

In silicon-vacancy (Si-$V$) centers in diamond, $\beta$ is more than 10 times smaller than $\alpha$ [41], so we can simplify $H_{\text{strain}}$ to the case where $\beta \to 0$ and $\alpha \to \chi_{\text{eff}}(\epsilon_{xx} - \epsilon_{yy})$ [Eq. (6)]. Then for a known $g_{\text{orb}}$ and a maximum magnetic field magnitude $|B|$, we can plot the required $B_z$ and $B_x$ versus the projected $g_{p,e}$ (Fig. 2). We are mostly interested in the regime $0 < |B| \le 0.18$ T, as this regime lies below $H_{c_1}$ of Nb. In Sec. III, we use the upper bound of 0.18 T for simulations. Above this critical field, we would incur additional losses in the coupled system due to the presence of

normal currents in the superconducting circuit. As higher-$H_{c_1}$ superconductors are explored as SC qubit materials, higher-$|B|$ regimes will become accessible to this scheme.
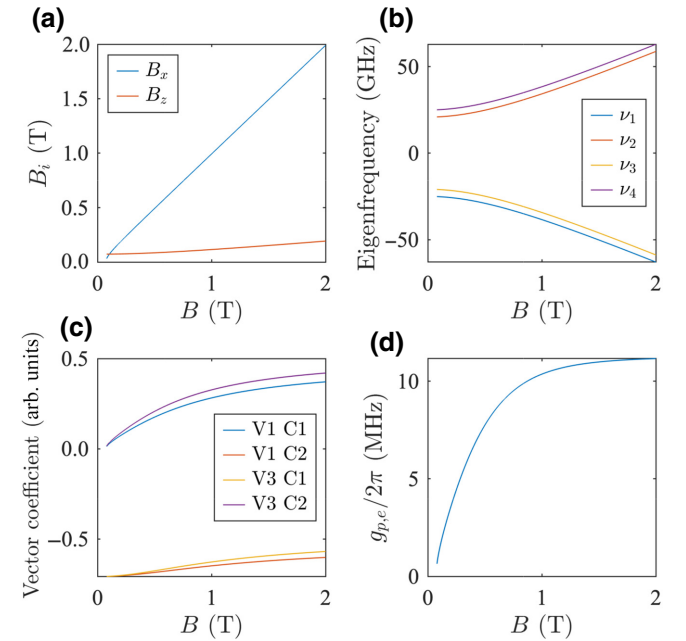


FIG. 2. Effect of the maximum applicable magnetic field on various parameters of the system. (a) Evolution of $B_x$ and $B_z$ required to maintain 4.31-GHz spin splitting as a function of $|B|$. (b) Change in eigenfrequencies as a function of $|B|$, where $\nu_1$ and $\nu_3$ are the eigenfrequencies of $|\psi_1\rangle$ and $|\psi_3\rangle$, the ground-state qubit levels of interest. (c) Change in the components $CN$ of vectors $|\psi_1\rangle$ and $|\psi_3\rangle$ with $|B|$, indicating greater spin-orbit mixing as the maximum applicable magnetic field increases. (d) Projected $g_{p,e}$ versus $|B|$ as determined by Eq. (17).

We must consider the coupling between the superconducting circuit and the electron spin to all acoustic modes supported by the piezoelectric resonator. The Hamiltonian describing this interaction can be written as

$$
\frac{\hat{H}}{\hbar} = \frac{\omega_{SC}}{2}\hat{\sigma}_{SC}^z + \sum_k \omega_{p,k}\hat{a}_{p,k}^\dagger \hat{a}_{p,k} + \frac{\omega_e}{2}\hat{\sigma}_e^z
$$
$$
+ \sum_k g_{SC,p;k}\left(\hat{\sigma}_{SC}^+ + \hat{\sigma}_{SC}^-\right)\left(\hat{a}_{p,k} + \hat{a}_{p,k}^\dagger\right)
$$
$$
+ \sum_k g_{p,e;k}\left(\hat{\sigma}_e^+ + \hat{\sigma}_e^-\right)\left(\hat{a}_{p,k} + \hat{a}_{p,k}^\dagger\right), \quad (20)
$$

where the index $k$ labels each acoustic mode and $\omega_{p,0}$ is the frequency of the resonator mode of interest. We can shift to a interaction picture by applying the transformation $\hat{H}' = \hat{U}\hat{H}\hat{U}^\dagger + i\dot{\hat{U}}\hat{U}^\dagger$, where $\hat{U} = \exp\left[i\left((\omega_{SC}/2)\hat{\sigma}_{SC}^z + \sum_k \omega_{p,k}\hat{a}_{p,k}^\dagger \hat{a}_{p,k} + (\omega_e/2)\hat{\sigma}_e^z\right)t\right]$. This transformation gives

$$
\frac{\hat{H}'}{\hbar} = \sum_k g_{SC,p;k}\left(e^{i(\omega_{SC}-\omega_{p,k})t}\hat{\sigma}_{SC}^+\hat{a}_{p,k}\right.
$$
$$
+ e^{-i(\omega_{SC}-\omega_{p,k})t}\hat{\sigma}_{SC}^-\hat{a}_{p,k}^\dagger\Big)
$$
$$
+ \sum_k g_{p,e;k}\left(e^{i(\omega_e-\omega_{p,k})t}\hat{\sigma}_e^+\hat{a}_{p,k}\right.
$$
$$
+ e^{-i(\omega_e-\omega_{p,k})t}\hat{\sigma}_e^-\hat{a}_{p,k}^\dagger\Big). \quad (21)
$$

We would like to determine the conditions in which we can ignore all resonator modes except the mode of interest, which we call "$k_0$" with frequency $\omega_{p,k_0}$. Let us first ignore the spin-phonon coupling and focus on the SC-phonon coupling. In the interaction Hamiltonian in Eq. (21), we can see that when $\omega_{SC} = \omega_{p,k_0}$ (the frequency of the acoustic resonator mode of interest), Rabi oscillations will be induced between the two modes. We would also, however, like to consider the oscillations induced between the superconducting circuit and the other resonator modes. Let us select a different transformation $\hat{H}_2' = \hat{U}_2\hat{H}\hat{U}_2^\dagger + i\dot{\hat{U}}_2\hat{U}_2^\dagger$, where $\hat{U}_2 = \exp\left[i\left((\omega_{SC}/2)\hat{\sigma}_{SC}^z + \sum_k \left(\omega_{p,k} + \Delta_{p,k}\right)\hat{a}_{p,k}^\dagger \hat{a}_{p,k}\right)t\right]$, where $\Delta_{p,k} \equiv \omega_{SC} - \omega_{p,k}$, and ignore the electron-spin-related terms. The resulting interaction Hamiltonian is

$$
\frac{\hat{H}_2'}{\hbar} = -\sum_k \Delta_{p,k}\hat{a}_{p,k}^\dagger \hat{a}_{p,k} + \sum_k g_{SC,p;k}\left(\hat{\sigma}_{SC}^+\hat{a}_{p,k} + \hat{\sigma}_{SC}^-\hat{a}_{p,k}^\dagger\right). \quad (22)
$$

The Heisenberg equations of motion for $\hat{\sigma}_{SC}$ and $\hat{a}_{p,k}$ are

$$
\dot{\hat{\sigma}}_{SC}^- = -\frac{i}{\hbar}\left[\hat{H}_2', \hat{\sigma}_{SC}^-\right] \quad (23)
$$
$$
= -\frac{\kappa_{SC}}{2}\hat{\sigma}_{SC}^- - ig_{SC,p;k_0}\hat{a}_{p,k_0} - i\sum_{k\neq k_0} g_{SC,p;k}\hat{a}_{p,k}, \quad (24)
$$
$$
\dot{\hat{a}}_{p,k} = -\frac{i}{\hbar}\left[\hat{H}_2', \hat{a}_{p,k}\right] \quad (25)
$$
$$
= \left(-i\Delta_{p,k} - \frac{\kappa_{p,k}}{2}\right)\hat{a}_{p,k} + ig_{SC,p;k}\hat{\sigma}_{SC}^-, \quad (26)
$$

where $g_{SC,p;k_0}$ is the desired acoustic mode's electromechanical coupling. In matrix form, this becomes

$$
\begin{bmatrix} \dot{\hat{\sigma}}_{SC} \\ \dot{\hat{a}}_{p,1} \\ \dot{\hat{a}}_{p,2} \\ \vdots \\ \dot{\hat{a}}_{p,N} \end{bmatrix} = \begin{bmatrix} -\frac{\kappa_{SC}}{2} & -ig_1 & -ig_2 & \cdots & -ig_N \\ ig_1 & C_1 & 0 & \ddots & 0 \\ ig_2 & 0 & C_2 & \ddots & 0 \\ \vdots & \ddots & \ddots & \ddots & \vdots \\ ig_N & \cdots & \cdots & \cdots & C_N \end{bmatrix} \begin{bmatrix} \hat{\sigma}_{SC} \\ \hat{a}_{p,1} \\ \hat{a}_{p,2} \\ \vdots \\ \hat{a}_{p,N} \end{bmatrix}, \quad (27)
$$

where $g_n = g_{SC,p;n}$ and $C_n = (-i\Delta_{p,n} - \kappa_{p,n}/2)$. This is equivalent to inducing Rabi oscillations of various frequencies and suppressions between the SC qubit and acoustic modes. The probability amplitude of population transfer to each acoustic mode from an excited SC state becomes

$$
\langle \sigma_{SC,k} \rangle = \frac{4(g_{SC,p;k})^2}{4(g_{SC,p;k}^2) + \left| \Delta_{p,k} + i\left(\frac{\kappa_{SC}+\kappa_{p,k}}{2}\right)\right|^2}
$$
$$
\times \sin^2\left(\frac{\sqrt{4\left(g_{SC,p;k}\right)^2 + \left|\Delta_{p,k}+i\left(\frac{\kappa_{SC}+\kappa_{p,k}}{2}\right)\right|^2}}{2}t\right). \quad (28)
$$

This gives us a SC qubit probability of being in the excited state as a function of time:

$$
\hat{\sigma}_{SC} = \sum_k \langle \sigma_{SC,k} \rangle
$$
$$
= \sum_k \frac{4(g_{SC,p;k})^2}{4\left(g_{SC,p;k}\right)^2 + \left(\Delta_{p,k} + i\left(\frac{\kappa_{SC}+\kappa_{p,k}}{2}\right)\right)^2}
$$
$$
\times \sin^2\left(\frac{\sqrt{4\left(g_{SC,p;k}\right)^2 + \left|\Delta_{p,k} + i\left(\frac{\kappa_{SC}+\kappa_{p,k}}{2}\right)\right|^2}}{2}t\right). \quad (29)
$$

The sum over all $\langle \sigma_{\mathrm{SC},k} \rangle$ with $k \neq k_0$ is a worst-case bound on the probability amplitude that could escape the computational basis into undesired acoustic modes, limiting state fidelity. If $\langle \sigma_{\mathrm{SC},k_0} \rangle / \sum_{k \neq k_0} \langle \sigma_{\mathrm{SC},k} \rangle \gg 1$, then we can effectively treat our system as having only one acoustic mode coupled to a SC qubit. The same physics governs the spin-phonon dynamics, replacing the appropriate couplings in Eqs. (28) and (29).

In the event that we can simplify the system dynamics to a single mechanical mode coupling to the transmon and the electron spin, the total system Hamiltonian becomes

$$
\begin{aligned}
\frac{\hat{H}}{\hbar} &= \frac{\omega_{\mathrm{SC}}}{2}\hat{\sigma}_{\mathrm{SC}}^z + \omega_p \hat{a}_p^\dagger \hat{a}_p + \frac{\omega_e}{2}\hat{\sigma}_e^z \\
&\quad + g_{\mathrm{SC},p}\left(\hat{\sigma}_{\mathrm{SC}}^+ \hat{a}_p + \hat{\sigma}_{\mathrm{SC}}^- \hat{a}_p^\dagger\right) + g_{p,e}\left(\hat{\sigma}_e^+ \hat{a}_p + \hat{\sigma}_e^- \hat{a}_p^\dagger\right).
\end{aligned}
$$
$$(30)$$

Here, the SC frequency $\omega_{\mathrm{SC}}$ is defined by the transmon Josephson and shunt capacitances, the spin frequency $\omega_e$ is given by the Zeeman splitting of the electron spin states, and the acoustic frequency $\omega_p$ is defined by the acoustic resonator geometry. The first three terms of this equation describe the energies of the uncoupled modes of the devices [Figs. 1(a)–1(c)], while the fourth and fifth terms describe the interaction dynamics. Generally, SCs feature $\omega_{\mathrm{SC}} \sim 4$–6 GHz [42]. Electron spin resonant frequencies can be arbitrarily set by an external magnetic field; to match this frequency range, fields of approximately 0.1 T are required [40]. The coupling coefficient $g_{\mathrm{SC},p}$ is physically governed by the piezoelectric effect, whereby a strain field produces an electric response, and vice versa [Fig. 1(d)]. This interaction is described by the strain-charge equations

$$S_{ij} = s_{ijkl}T_{kl} + d_{kij}E_k, \qquad (31)$$

$$D_i = d_{ijk}T_{jk} + \epsilon_{ik}E_k, \qquad (32)$$

where $s_{ijkl}$ and $d_{ijk}$ are the elastic and piezoelectric coefficient tensors of the resonator's piezoelectric material, $S_{ij}$ and $T_{ij}$ are the stress and strain fields, and $E_i$ and $D_i$ are the electric and displacement fields. Given a spatial electric field profile $\mathbf{E}_{\mathrm{IDT}}(\mathbf{r})$ produced by some arbitrary voltage $V_{\mathrm{app}}$ across the interdigital transducer (IDT), the normalized single quantum electric field is given by [43]

$$
\mathbf{e}_{\mathrm{SC}}(\mathbf{r}) = \sqrt{\left(\frac{\hbar\omega_{\mathrm{SC}}}{(C_S + C_J + C_{\mathrm{IDT}})\,V_{\mathrm{app}}^2/2}\right)}\mathbf{E}_{\mathrm{IDT}}(\mathbf{r})e^{-i\omega_{\mathrm{SC}}t},
$$
$$(33)$$

where the capacitances are indicated in Fig. 1. Since $C_S$ is typically much larger than $C_{\mathrm{IDT}}$ and $C_J$ for transmon qubits, the MW-photon energy is largely contained in

$C_S$. Similarly, for a strain profile $\mathbf{T}_p(\mathbf{r})$ produced by an arbitrary mechanical displacement, the normalized single-phonon strain field is given by [43]

$$
\mathbf{t}_p(\mathbf{r}) = \sqrt{\left(\frac{\hbar\omega_p}{\int_V dV\, \mathbf{s}(\mathbf{r})|\mathbf{T}_p(\mathbf{r})|^2/2}\right)}\mathbf{T}_p(\mathbf{r})e^{-i\omega_p t}, \quad (34)
$$

where $\mathbf{s}(\mathbf{r})$ is the elastic tensor at position $\mathbf{r}$. Following Eq. (32), $\mathbf{t}_p(\mathbf{r})$ will produce an electric displacement field given by $\mathbf{d} \cdot \mathbf{t}_p(\mathbf{r})$, where $\mathbf{d}$ is the piezoelectric coefficient tensor. Then the coupling $g_{\mathrm{SC},p}$ will be determined by the overlap integral between $\mathbf{e}_{\mathrm{SC}}(\mathbf{r})$ and $\mathbf{d} \cdot \mathbf{t}_p(\mathbf{r})$ [44],

$$
g_{\mathrm{SC},p} = \frac{1}{2\hbar}\int_V dV \left(\mathbf{t}_p^*(\mathbf{r}) \cdot \mathbf{d}^T \cdot \mathbf{e}_{\mathrm{SC}}(\mathbf{r}) + \mathbf{e}_{\mathrm{SC}}^*(\mathbf{r}) \cdot \mathbf{d} \cdot \mathbf{t}_p(\mathbf{r})\right).
$$
$$(35)$$

The spin-phonon coupling $g_{p,e}$ results from the spin-strain susceptibility $\chi_{\mathrm{spin}}$ of quantum emitters in a strain field [40,41,45]. For a single-phonon strain profile $\mathbf{t}_p$, the resulting coupling $g_{\mathrm{spin}}(\mathbf{r}) = \chi_{\mathrm{spin}} \cdot \mathbf{t}_p(\mathbf{r})$. In group-IV emitters in diamond, $\chi_{\mathrm{spin}}$ depends on the spin-orbit mixing, which increases monotonically with an off-axis magnetic field, and primarily interacts with transverse strain in the emitter frame [40]. Therefore, for the rest of this analysis, we set this expression to be

$$
g_{p,e}(\mathbf{r}) = \chi_{\mathrm{eff}}(t_{xx}'(\mathbf{r}) - t_{yy}'(\mathbf{r})), \qquad (36)
$$

where $\mathbf{t}'(\mathbf{r})$ is the single-phonon strain profile in the coordinate system of the emitter and $\chi_{\mathrm{eff}} \approx 0.28$ PHz/$\epsilon$, where $\epsilon$ is 1 unit strain [41].

## III. TRANSDUCER DESIGN

To implement the device in Fig. 1, we require a platform with (i) superconductivity, (ii) piezoelectricity, (iii) acoustic cavities, and (iv) strain transfer to diamond emitters. To address the first-two requirements, we propose a silicon-on-insulator (SOI) platform with a thin-film deposition of $\mathrm{Sc}_{0.32}\mathrm{Al}_{0.68}\mathrm{N}$. This material system allows superconducting qubits and piezoelectric materials to coinhabit one chip [46,47]. To address the last-two requirements, we codesign a Nb-on-$\mathrm{Sc}_{0.32}\mathrm{Al}_{0.68}\mathrm{N}$-on-SOI piezoelectric resonator with a heterogeneously integrated diamond thin membrane. We propose niobium as a well-characterized superconductor with high $H_{c1} = 0.18$ T and $H_{c2} = 2$ T [48–50], as required for operation with the spin. Since $g_{p,e}$ monotonically increases with the magnetic field, we assume a static magnetic field of 0.18 T for the rest of this article. SOI platforms have been used for piezoelectric resonators [51,52], and diamond-AlN interfaces have been used to acoustically drive emitters in diamond [53–55]. $\mathrm{Sc}_{0.32}\mathrm{Al}_{0.68}\mathrm{N}$ further boosts the piezoelectric coefficient of AlN, allowing us to achieve a stronger interaction [56,57].
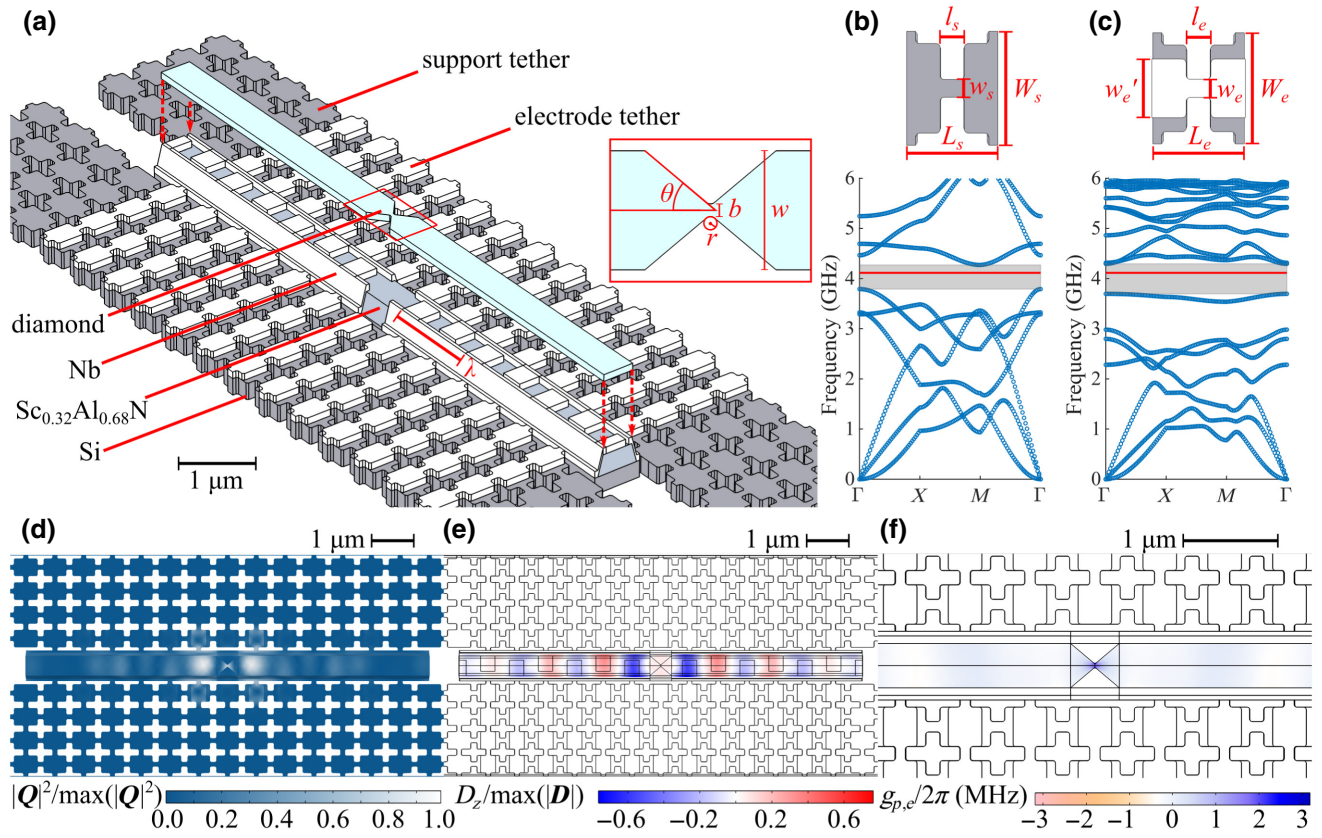
FIG. 3.    Electromechanical transducer design. (a) Lamb-wave resonator and relevant design parameters. The resonator geometry is parameterized by $\lambda = 1370$ nm, $w = 465$ nm, $t_d = 100$ nm, $t_{Al} = 100$ nm, $t_{Sc_{0.32}Al_{0.68}N} = 300$ nm, and $t_{Si} = 250$ nm ($t_i$ is the thickness of layer $i$), with the diamond taper defined by $b = 40$ nm, $r = 25$ nm, and $\theta = 50°$. The support tethers are defined by $W_s = 705$ nm, $L_s = 565$ nm, $w_s = 110$ nm, and $l_s = 150$ nm and the electrode tethers are defined by $W_e = 685$ nm, $L_e = 565$ nm, $w_e = 110$ nm, and $l_e = 150$ nm. (b),(c) Phononic band structure of the (b) support and (c) electrode tethers, with a 500-MHz band gap indicated in gray shading and the resonant frequency indicated by the red line. (d) Normalized mechanical displacement of the resonator. (e) Induced piezoelectric displacement field at the central slice of the $Sc_{0.32}Al_{0.68}N$ layer. (f) Spatial profile of $g_{p,e}$ at the center slice of the diamond layer, assuming a magnetic field of 0.18 T.

We present the resonator design in Fig. 3. Our device is based on Lamb-wave resonators, which produce standing acoustic waves dependent on IDT electrode periodicity $\lambda$ and material thickness [58–60]. We localize the strain in the diamond thin film using a fabrication-limited central taper [Fig. 3(a), inset] [61]. To maintain high quality factors, we tether the Lamb-wave resonator via phononic crystal tethers placed at displacement nodes of the box [43]. We further propose an angled $Sc_{0.32}Al_{0.68}N$ sidewall in the transducer (15° from the normal) that allows the electrodes to "climb" on top of the $Sc_{0.32}Al_{0.68}N$ film, rather than requiring a continuous piezoelectric layer over the phononic tethers. The selected $Sc_{0.32}Al_{0.68}N$ and phononic tether parameters outlined in Fig. 3 facilitate the design of wide-band-gap phononic tethers and are compatible with current fabrication techniques and tolerances [43,62–65].

We simulate device performance using the finite-element method (FEM) in COMSOL MULTIPHYSICS to produce the phononic tether band structures and mode profiles [Figs. 3(b)–3(e)]. The tether band structure exhibits a 500-MHz band gap around the device's approximately-4.11-GHz resonant mode. This frequency is desirable as it falls near the central operating range of most superconducting qubits [42]. Additionally, the 4.11-GHz resonant mode is itself isolated from other acoustic modes of the system by approximately 56 MHz, which is enough for us to ignore parasitic couplings and treat the transducer in the single-mode approximation (Fig. 4). Figures 3(d) and 3(e) show the mechanical and electrical displacement fields of this mode, from which we derive $\mathbf{e}_{SC}(\mathbf{r})$ and $\mathbf{t}_p(\mathbf{r})$, respectively. We calculate $g_{SC,p} \approx 7.0$–20.5 MHz (for a shunt capacitance of 65–190 fF, corresponding to 100 MHz $< E_C/h <$ 300 MHz [42]) and a maximum $g_{p,e} \approx 3.2$ MHz according to Eqs. (35) and (36). The strain maximum occurs at the edges of the central diamond taper, which maximizes $g_{p,e}$ [Fig. 3(f)]. We simulate the expected mechanical quality factor of the 4.11-GHz mode as a function of the number
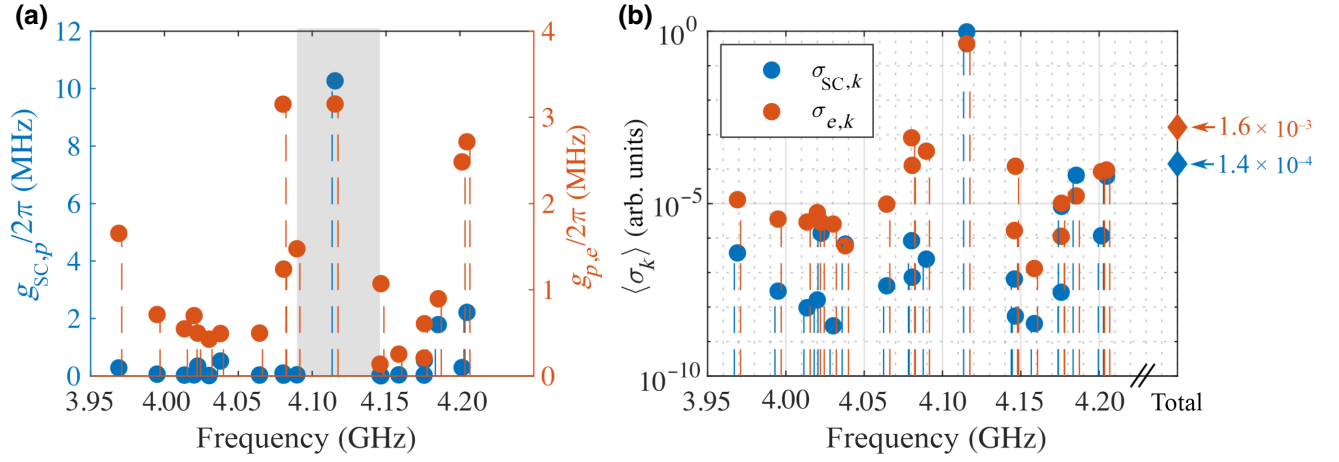
FIG. 4.    Electromechanical and spin-mechanical couplings and population transfer to each acoustic mode. (a) An approximately-56-MHz frequency window (gray shaded region) in which our mode of interest (approximately 4.115 GHz) lies. The couplings $g_{\mathrm{SC},pi}$ and $g_{p,ei}$ are plotted for each mode, assuming a shunt capacitance $C_S \sim 130$ fF and a magnetic field of 0.18 T. (b) The Rabi-population-transfer probability from the superconducting circuit and electron spin to each acoustic mode [see Eq. (28)], showing a combined mode suppression (diamond markers) of at least 3 orders of magnitude.

of phononic tether periods (Fig. 5) and find that, for around five tether periods or more, the mechanical mode will have a sufficient expected $Q$ of $10^5$ or higher.

### IV. QUANTUM STATE TRANSFER

In Fig. 6, we explore different protocols for quantum transduction from an initialized SC to a spin. The time evolution of the system when initialized in the $\rho_0 = |100\rangle\langle100|$ state (where the indices consecutively refer to the state of the SC, the Fock state of the phonon, and the $z$ projection of the spin) is calculated with use of the Lindblad master equation,

$$\frac{d}{dt}\rho = -\frac{i}{\hbar}[\rho, \hat{H}(t)] + \mathcal{D}[\Theta(T)]\rho + \mathcal{D}[\Gamma(T)]\rho, \quad (37)$$

where the Hamiltonian in a frame rotating at rate $\omega_p$ is

$$\begin{aligned}
\frac{\hat{H}(t)}{\hbar} &= \frac{\Delta_{\mathrm{SC}}(t)}{2}\hat{\sigma}_{\mathrm{SC}}^z + \frac{\Delta_e(t)}{2}\hat{\sigma}_e^z \\
&\quad + g_{\mathrm{SC},p}\left(\hat{\sigma}_{\mathrm{SC}}^+\hat{a}_p + \hat{\sigma}_{\mathrm{SC}}^-\hat{a}_p^\dagger\right) + g_{p,e}\left(\hat{\sigma}_e^+\hat{a}_p + \hat{\sigma}_e^-\hat{a}_p^\dagger\right).
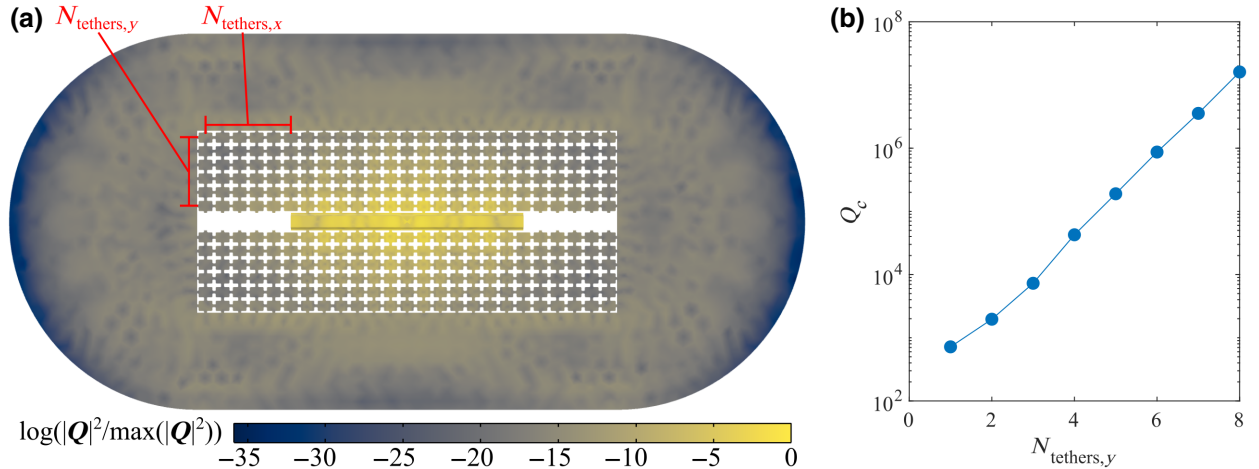\end{aligned}$$
$$(38)$$



FIG. 5.    FEM simulation of the piezoelectric transducer with phononic tethers and surrounding bulk treated as perfectly matched layers to simulate clamping quality factor $Q_c$. (a) Simulated mechanical-mode profile with $\log(|\mathbf{Q}|^2/\max(|\mathbf{Q}|^2))$ plotted to show energy concentration in the resonator, since energy scales with the square of mechanical displacement. In this simulation, the free parameter $N_{\mathrm{tethers},y} = N_{\mathrm{tethers},x}$, where $N_{\mathrm{tethers},y}$ and $N_{\mathrm{tethers},x}$ indicate the number of phononic mode tether periods normal and parallel to the resonator edge from the resonator to the bulk Si layer, respectively. (b) $Q_c$ versus $N_{\mathrm{tethers},y}$ for the 4.11-GHz resonator mode of interest.
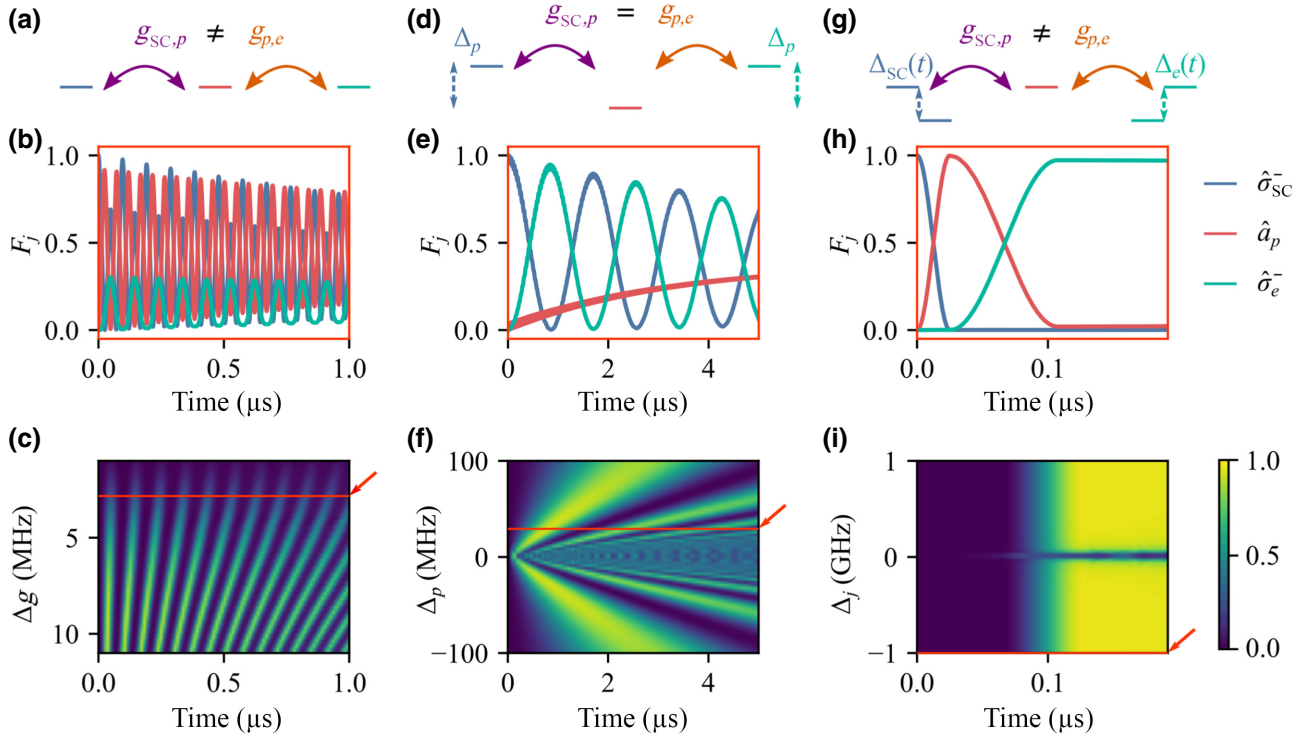
FIG. 6. Analysis of the coupled SC-phonon-spin system under different protocols: (a)–(c) uncontrolled time evolution, when all modes are on resonance and coupling rates are maximized; (d)–(f) time evolution detuned from the acoustic resonance, which allows state transfer through virtual phonon excitation; and (g)–(h) time evolution under detuning control, which allows controlled Rabi flops across the modes. (b),(e),(h) The population dynamics of each mode for the aforementioned protocols. (c),(f),(i) The spin population over time for the variable parameter of the procedure, with operational points for (b),(e),(h) indicated with orange lines: (c) the population for a given $\Delta g$; (f) the population for achievable phonon detuning $\Delta_p$; (i) performance for unused mode detuning $\Delta_i$ during each Rabi swap.

The superoperator $\mathcal{D}$ is given by

$$\mathcal{D}[c]\rho = \frac{1}{2}\left(2c\rho c^\dagger - c^\dagger c\rho - \rho c^\dagger c\right), \qquad (39)$$

and

$$\Theta(T) = \sum_{\sigma_i \in \{\hat{a}_p, \hat{\sigma}_{SC}^-, \hat{\sigma}_e^-\}} \sqrt{\kappa_i[n_{T_i}(\omega_i) + 1]}\sigma_i, \qquad (40)$$

$$\Gamma(T) = \sum_{\sigma_i \in \{\hat{a}_p, \hat{\sigma}_{SC}^-, \hat{\sigma}_e^-\}} \sqrt{\kappa_i[n_{T_i}(\omega_i)]}\sigma_i^\dagger. \qquad (41)$$

Here, $\Delta_{SC}(t) \equiv \omega_{SC}(t) - \omega_p$ is the superconducting-qubit detuning, $\Delta_e(t) \equiv \omega_e(t) - \omega_p$ is the spin detuning at time $t$, and $n_{T_i}(\omega_i)$ is the thermal occupancy of the $i$th mode (we assume $T = 0.015$ K in our simulations). The use of time-varying detuning can be easily implemented, for example, via on-chip flux bias lines [66–68], unlike time-varying coupling rates explored in previous work [20]. We account for dephasing in each mode with conservative estimates of decoherence rates $\kappa_{SC}/2\pi = 10$ kHz, $\kappa_p/2\pi = \omega_p/2\pi Q \approx 40$ kHz, and $\kappa_e/2\pi = 100$ kHz [38,39,69–71].

As cryogenic operation of $Sc_{0.32}Al_{0.68}N$-on-SOI acoustic resonators—as well as diamond hybrid intergration on said devices—has not been previously explored, we further discuss prospects for $Q_{mech}$ below.

Figures 6(b), 6(e), and 6(h) show the state transfer fidelity $F_j \equiv \langle\psi_j|\rho(t)|\psi_j\rangle$ plotted versus the target state $|\psi_j\rangle = |1_j\rangle$ under different conditions. In Fig. 6(a), where the modes are all resonant ($\omega_{SC} = \omega_p = \omega_e = 4.11$ GHz) and $g_{SC,p}/2\pi = 10$ MHz, $F_e$ is low due to the mismatch $\Delta g(g_{p,e}) = g_{SC,p} - g_{p,e}$ [Fig. 6(c)]. Assuming one reduces $g_{SC,p}$ or $g_{p,e}$, for example, by increasing the qubit shunt capacitance $C_S$ or reducing the transverse magnetic field, $F_e$ may increase at the cost of maximum coupling rates.

For Fig. 6(b), we detune the phonon mode by $\Delta_p \equiv \omega_p - \omega_{SC}$, where $\omega_{SC} = \omega_e$, and keep the coupling rates matched at 3.0 MHz. In this case, $F_e \sim 0.95$ via virtual excitation of the phonon mode, if the phonon mode is detuned by 30 MHz. This protocol generates a very low population in the phonon mode, primarily exchanging states between the superconducting qubit and the spin. If the phonon mode is lossy, this transduction method is preferred. However, while this protocol features wider efficiency peaks in time, which may require less-stringent

pulse control [see Fig. 6(e)], it does not overcome the issue of coupling imbalance, and additionally suffers from decoherence of the superconducting-qubit and spin modes over a longer protocol time [Fig. 6(f)].

Figure 6(g) shows the optimal solution, assuming control over $\Delta_{SC}(t)$ and $\Delta_e(t)$, in a double-Rabi-flop protocol. During this protocol, it is assumed that $g_{SC,p}/2\pi = 10$ MHz (which overcomes losses during the Rabi flop, while still allowing mode isolation during the next flop) and $g_{p,e}/2\pi = 3.0$ MHz. We also assume $\Delta_{SC}(t) = 0$ and $0$ MHz $\leq \Delta_e(t) \leq 1$ GHz for $t \in \{0, \pi/(2g_{SC,p})\}$—the duration of a Rabi flop between the SC and the phonon. Then, $\Delta_{SC}(t) = \Delta_e(t = 0)$ MHz and $\Delta_e(t) = 0$ for $t \in \{\pi/(2g_{SC,p}), \pi/(2g_{SC,p}) + \pi/(2g_{p,e})\}$—the duration of a Rabi flop between the phonon and the spin. This sequentially transfers states between the modes [Fig. 6(h)], and for $\Delta_e(t = 0) > 500$ MHz can achieve $F_e > 0.97$ [Fig. 6(i); for $\Delta_j = 1.0$ GHz, $F_e = 0.971$]. In this protocol, we ignore the losses that can occur when one varying $\Delta_{SC}$ and $\Delta_e$. In reality, one has to select a pair of $\Delta_{SC}$ and $\Delta_e$ that do not fall on resonance with another acoustic mode of the system to prevent Rabi oscillations between the SC qubit or the electron spin and an undesired acoustic mode.

Each of these scenarios achieves transduction to the spin with high fidelity. The third scenario allows the quantum state to persist in the spin without continued interaction with the acoustic or SC modes. While in this state, the electron spin can access other degrees of freedom (e.g., $^{13}$C spins [72,73]).

There are three sources of loss (described by quality factors) that we may consider in our piezoelectric transducer. First, we consider the clamping quality factor $Q_c$, which we can engineer to be nonlimiting as shown in Fig. 5. Next, we note the Akhiezer-loss-related $Q_A$ [74], which we expect to be $10^7$ or higher at millikelvin temperatures, is negligible [75,76]. Finally, $Q_{TLS,l}$—the $l$th material's TLS-related $Q$—is harder to predict. These $Q$ values depend on the number of quasiparticles or TLSs trapped in each of the device's material interfaces [77] and are weighted by the electric field participation $p_i$ in each interface, and in comparable microscale or nanoscale systems, TLS loss has been limited to approximately $10^4$–$10^5$ [77,78]. Considering these three sources of loss, $Q_{mech}$ is the inverse sum of the three quality-factor sources,

$$Q_{mech} = \left( Q_c^{-1} + \sum_l p_i \left( Q_{TLS,l} \right)^{-1} + Q_A^{-1} \right)^{-1}. \quad (42)$$

We define the regimes of $Q_{mech}$ where each protocol from Fig. 7 has the highest $F_e$ as follows:

(i)  If $Q_{mech} \lesssim 2 \times 10^4$, protocol 2 is superior.
(ii)  If $2 \times 10^4 \lesssim Q_{mech} \lesssim 4 \times 10^5$, protocol 1 is superior.
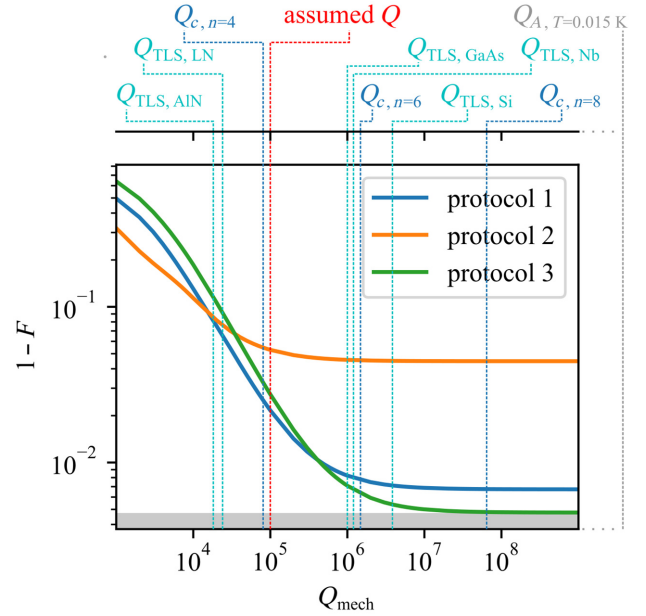


FIG. 7.   Sweep of protocol performance as a function of the total quality factor of the mechanical resonator. TLS-limited $Q$ values—which are inherent to the materials used in the pizeo-electric nanocavity—for Si [79,80], AlN [78], Nb [81], and alternatives in GaAs [81] and lithium niobate (LN) [77] are in cyan. The device's clamping-limited $Q$ values as a function of tether number–which determines the phononic mode isolation from the bulk chip–are given in blue. Akhiezer losses (gray) are nondominant at $T = 0.015$ K. Finally, our assumed $Q \approx 10^5$ for the simulations in Fig. 3 is in red. The $F > 0.995$ regime (dark gray) requires better SCs and spins for it to be achieved.

(iii)  If $4 \times 10^5 \lesssim Q_{mech}$, protocol 3 is superior.

We note that $Q_{TLS}$ likely dominates $Q_{mech}$ more than fabrication imperfections (which fall under $Q_c$) or errors due to heating at millikelvin temperatures. Given this uncertainty in $Q_{TLS}$ and therefore $Q_{mech}$, the greatest challenge in reaching $F_e \gtrsim 0.99$ is reducing TLS loss in the piezoelectric layer, as indicated by published intrinsic quality factors of, for example, monolithic aluminum nitride or lithium niobate resonators [77,78]. So, while current hardware may encourage us to use the virtual coupling protocol for coupling through a lossy intermediary phononic mode, future iterations of this scheme with improved materials and interfaces yielding $Q_{mech} \gtrsim 10^6$ can expect to break the 0.99 transduction fidelity barrier with use of a resonant protocol, which would surpass the 1% thresholds of known quantum error correction codes and thus be compatible with scalable quantum information processing schemes [82–84].

## V. ANALYSIS OF SPIN-REGISTER SYSTEM

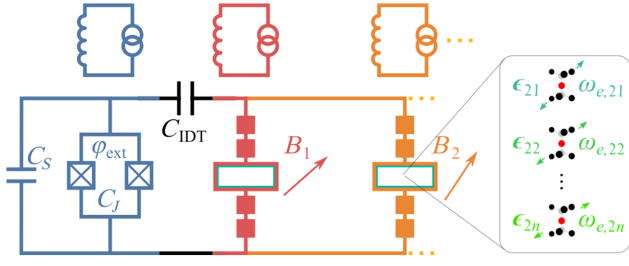In Fig. 8, we present a road map to scaling this architecture to form a memory register for superconducting

FIG. 8. Scaling the schematic to a quantum memory register. By implanting $n$ emitters in each of $m$ detuned mechanical resonators in parallel with the superconducting qubit of interest, one can create an efficient interface with an $m \times n$ optically addressable ancilla register.

circuits. Since the shunt capacitance far exceeds the capacitance of a single IDT, additional electromechanical resonators in parallel to a single transmon qubit do not significantly change the rates of coupling to each resonator. Individual control over each resonator can be obtained with electrical switching of contacts to each resonator (e.g., by cryo-MEMS) [85,86]. If this is not possible, controls can still be obtained in the frequency domain if each resonator frequency is sufficiently detuned from all others and is within the tunability range of the transmon. This gives two constraints on the number of parallel resonators we can add: the maximum number of resonators before $g_{SC,p}$ for each resonator drops below a desired value, and the maximum number of resonators before the frequency spectrum becomes overcrowded.

From electrostatic simulations in COMSOL MULTI-PHYSICS, $C_S \approx 70 C_{IDT}$, allowing us to add around ten resonators in parallel without decreasing the coupling to each resonator by more than 15%. Additionally, each resonator can house several quantum emitters, which themselves will be operating at different frequencies $\omega_{e,ij}$ due to differing magnetic field and strain environments creating a unique Zeeman effect for each color center. Assuming one implants $n$ emitters in each resonator, this creates an easily accessible $m \times n$ register of ancillas for a single transmon.

We would like to evaluate overcrowding of the frequency spectrum in this picture. In an ideal case, when we tune the superconducting circuit on resonance with a mechanical mode $\omega_m$, we would like the circuit to be approximately coupled to *only* that acoustic mode. This is the same condition as we present in Sec. II to assume that we can simplify the dynamics of the SC-phonon-spin system to that of coupling via a single acoustic mode. Similarly, we would like to determine the condition where we can assume each piezoelectric resonator can individually couple to a single spin. Assuming that each of the $m$ resonators has only a single mode coupled to the SC qubit, the full Hamiltonian describing the $m$ resonator, $m \times n$ spin

system is

$$
\begin{aligned}
H_\Sigma = {} & \frac{\omega_{SC}}{2}\hat{\sigma}^z_{SC} + \sum_{i=1}^{m}\sum_{j=1}^{n}\left[\omega_{p,i}\hat{a}^\dagger_{p,i}\hat{a}_{p,i} + \frac{\omega_{e_{ij}}}{2}\hat{\sigma}^z_{e_{ij}}\right.\\
& + g_{SC,p_i}\left(\hat{\sigma}^+_{SC}\hat{a}_{p,i} + \hat{\sigma}^-_{SC}\hat{a}^\dagger_{p,i}\right)\\
& \left. + g_{p,e_{ij}}\left(\hat{\sigma}^+_{e_{ij}}\hat{a}_{p,i} + \hat{\sigma}^-_{e_{ij}}\hat{a}^\dagger_{p,i}\right)\right].
\end{aligned}
\tag{43}
$$

Following exactly from Eqs. (28) and (29), the required condition for assuming electromechanical coupling to just the $i_0$th of $m$ resonators is that

$$
\begin{aligned}
& \sum_{i\neq i_0}^{m}\langle\sigma_{SC,i}\rangle \\
&= \sum_{i\neq i_0}^{m}\frac{4(g_{SC,p;i})^2}{4(g^2_{SC,p;i}) + \left|\Delta_{p,i} + i\left(\frac{\kappa_{SC}+\kappa_{p,i}}{2}\right)\right|^2}\\
&\quad \times \sin^2\left(\frac{\sqrt{4\left(g_{SC,p;i}\right)^2 + \left|\Delta_{p,i} + i\left(\frac{\kappa_{SC}+\kappa_{p,i}}{2}\right)\right|^2}}{2}t\right)\\
&\quad \ll \langle\sigma_{SC,i_0}\rangle.
\end{aligned}
\tag{44}
$$

Similarly, after swapping the population into one of the resonator modes, the condition for assuming spin-mechanical coupling to just the $j_0$th of $n$ electron spins is that

$$
\begin{aligned}
\sum_{j\neq j_0}^{n}\langle\sigma_{e,j}\rangle &= \sum_{j\neq j_0}^{n}\frac{4(g_{p,e;j})^2}{4(g^2_{p,e;j}) + \left|\Delta_{p,j} + i\left(\frac{\kappa_e+\kappa_{p,j}}{2}\right)\right|^2}\\
&\quad \times \sin^2\left(\frac{\sqrt{4\left(g_{p,e;j}\right)^2 + \left|\Delta_{p,j} + i\left(\frac{\kappa_e+\kappa_{p,j}}{2}\right)\right|^2}}{2}t\right)\\
&\quad \ll \langle\sigma_{e,j_0}\rangle.
\end{aligned}
\tag{45}
$$

We can see from the spin-phonon coupling points in Fig. 4 that frequency crowding can begin to promote Rabi oscillations with populations on the order of $10^{-3}$ of the desired mode when within a 100-MHz frequency window. So parallelization of spins in one resonator would require changing the local magnetic field for each resonator and intelligent spacing of the emitters to promote a wide distribution of resonant frequencies, or sacrificing state-transfer fidelity to a single spin by overcrowding the simulated frequency window of operation. This is not as much of a problem given the order-of-magnitude superior mode suppression on the electromechanical side of the system.

Thus, we can comfortably parallelize around ten piezo-electric resonators to a single SC qubit and one to three emitters per resonator. When accounting for the surrounding $^{13}$C nuclear spins, we envision that this scaling method can provide a SC qubit with a ten-or-greater-nuclear-spin memory register.

## VI. IMPLEMENTING QUANTUM PROTOCOLS ON A TRIPARTITE SYSTEM

In Fig. 9, we describe the SWAP gate between a superconducting transmon and Si-$V$ electron spin implemented by our transduction protocols (specifically protocol 3). This consists of two SWAP gates first between the transmon and the transducer's phonon mode and next between the phonon mode and the electron spin. We propose that the first SWAP operation is initiated by the tuning of the flux bias of the transmon superconducting quantum interference device loop to tune the transmon in and out of resonance with the phononic mode [Eq. (1)] [42]. Similarly, an external magnetic field can be varied to tune the electron-spin transition in and out of resonance with the phonon to initiate the second SWAP gate [Eqs. (13)–(16)]. Once an excitation is transferred to the electron spin, then optical readout can be performed with a free-space laser tuned

to the electron-spin transition frequency. Note that the diffraction-limited spot size $d$ of a $\lambda = 620$ nm laser entering a high-numerical-aperture microscope—for example, a numerical aperture of 0.9—is around $\lambda/2\text{NA} = 344$ nm, which is smaller than the distance between two electrodes in our device. Therefore, we expect that a free-space laser should not cause excessive scattering.

Figure 10 shows how to use the transducer in a quantum computation scheme that combines distilled entanglement with computation and memory storage. First, one can initialize two systems in different dilution fridges featuring our transducer to the ground state and carry out a distilled-entanglement scheme using the SiV$^-$ electron spins and coupled $^{13}$C nuclear spins in each transducer [Fig. 10(a)] [87]. Next, one can implement a SWAP gate between the nuclear-spin and electron-spin qubits in each fridge via laser addressing, followed by a SWAP operation to each coupled transmon to transfer entanglement to the superconducting circuit. Computation can be done on an arbitrarily sized superconducting circuit to which each transmon is coupled [Fig. 10(b)]. Finally, a SWAP gate can be implemented between the coupled transmons and each nuclear spin to store the excited state in each fridge [Fig. 10(c)]. This proposal, when combined with the spin register in the previous section, provides a network interface and memory bank to superconducting quantum circuits.
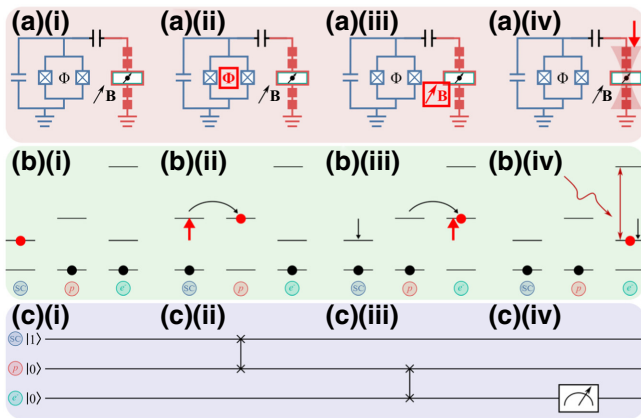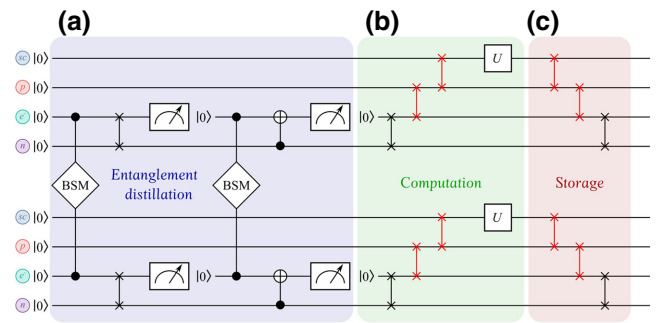


FIG. 9. Transduction protocol for optical readout of the coupled system. (a) The active control elements at each step, (b) energy-level diagram charting the physical movement of an excitation through the tripartite-coupled system, and (c) equivalent quantum gates on the three qubits. (i) An initialized state with the superconducting qubit in the excited state $|1\rangle$ and the phonon and the electron spin initialized to the ground state $|0\rangle$. (ii) The first SWAP operation, initiated by tuning the superconducting circuit flux to be on resonance with the phonon mode for half a Rabi oscillation cycle. (iii) The second SWAP operation, initiated by tuning the electron spin on resonance with the phonon mode via changing the external dc magnetic field. (iv) Laser addressing of the electron spin, which can be accomplished with a free-space microscope or by other means, allowing optical readout of the system [88].

FIG. 10. Implementation of the transducer in a quantum entanglement and computation protocol. (a) Entanglement distillation using a coupled $^{13}$C nuclear spin [87]. Here, "BSM" indicates a Bell-state measurement, the cross symbol represents a SWAP gate, the arrow represents a measurement operation, and the white circle with a cross represents a controlled NOT operation. (b) Use of SWAP gates to conduct computational operations using the superconducting qubit and any other superconducting qubits interacting with the one in the schematic (not shown). Here, our transducer would be used to implement the otherwise-missing SWAP gates, shown in red. The $U$ operation represents an arbitrary computation done with the superconducting qubit. (c) Information storage in a coupled $^{13}$C nuclear spin, where our transducer would again be used to implement the otherwise-missing SWAP gates (shown in red).

## VII. OUTLOOK

An open question remains regarding the bonding strength between the diamond thin film and the underlying resonator, which, if low, can incur additional losses. However, for single-phonon occupation, the van der Waals static frictional force exceeds the strain-generated force on the resonator.

Ultimately, we propose a resonator architecture capable of simultaneously coupling a microwave photonic mode from a superconducting circuit and an electronic spin from a solid-state color center to a single phonon. For our calculated coupling parameters and conservatively assumed $Q$ values across the three modes, we expect SC-phonon cooperativity $C_{SC,p} = 4g_{SC,p}^2/\kappa_{SC}\kappa_p \sim 4 \times 10^3$ and, similarly, spin-phonon cooperativity $C_{p,e} = 4g_{p,e}^2/\kappa_p\kappa_e \sim 10^2$. This doubly-strongly-coupled architecture has a number of uses. Firstly, it can provide superconducting-circuit qubits with access to a long-lived quantum memory in the form of a nuclear-spin register surrounding the electron spin. Secondly, this resonator can grant superconducting-circuit qubits a spin-photon interface for efficient coupling to fiber optical quantum networks. Finally, by multiplexing each SC with several acoustic resonators and each acoustic resonator with several spins, this architecture can yield a memory bank of quantum memories for computational superconducting circuits. We believe introducing this quantum transducer into existing superconducting circuits is a large step toward developing a specialized hybrid quantum computer with fast superconducting qubits for processing and slow, long-lived memory qubits in the solid state for storage and communication.

## ACKNOWLEDGMENTS

[1] P. Jurcevic, A. Javadi-Abhari, L. S. Bishop, I. Lauer, D. F. Bogorin, M. Brink, L. Capelluto, O. Günlük, T. Itoko, N. Kanazawa, *et al.*, Demonstration of quantum volume 64 on a superconducting quantum computing system, Quantum Sci. Technol. **6**, 025020 (2021).

[2] F. Arute, K. Arya, R. Babbush, D. Bacon, J. C. Bardin, R. Barends, S. Boixo, M. Broughton, B. B. Buckley, D. A. Buell, *et al.*, Hartree-Fock on a superconducting qubit quantum computer, Science **369**, 1084 (2020).

[3] M. Steiner, P. Neumann, J. Beck, F. Jelezko, and J. Wrachtrup, Universal enhancement of the optical readout fidelity of single electron spins at nitrogen-vacancy centers in diamond, Phys. Rev. B **81**, 035205 (2010).

[4] L. J. Rogers, K. D. Jahnke, M. H. Metsch, A. Sipahigil, J. M. Binder, T. Teraji, H. Sumiya, J. Isoya, M. D. Lukin, P. Hemmer, and F. Jelezko, All-Optical Initialization, Readout, and Coherent Preparation of Single Silicon-Vacancy Spins in Diamond, Phys. Rev. Lett. **113**, 263602 (2014).

[5] M. E. Trusheim, B. Pingault, N. H. Wan, M. Gündoğan, L. De Santis, R. Debroux, D. Gangloff, C. Purser, K. C. Chen, M. Walsh, *et al.*, Transform-Limited Photons from a Coherent Tin-Vacancy Spin in Diamond, Phys. Rev. Lett. **124**, 023602 (2020).

[6] M. K. Bhaskar, R. Riedinger, B. Machielse, D. S. Levonian, C. T. Nguyen, E. N. Knall, H. Park, D. Englund, M. Lončar, D. D. Sukachev, *et al.*, Experimental demonstration of memory-enhanced quantum communication, Nature **580**, 60 (2020).

[7] J. J. Pla, K. Y. Tan, J. P. Dehollain, W. H. Lim, J. J. Morton, F. A. Zwanenburg, D. N. Jamieson, A. S. Dzurak, and A. Morello, High-fidelity readout and control of a nuclear spin qubit in silicon, Nature **496**, 334 (2013).

[8] R. Nagy, M. Niethammer, M. Widmann, Y.-C. Chen, P. Udvarhelyi, C. Bonato, J. U. Hassan, R. Karhu, I. G. Ivanov, N. T. Son, *et al.*, High-fidelity spin and optical control of single silicon-vacancy centres in silicon carbide, Nat. Commun. **10**, 1 (2019).

[9] V. Ranjan, G. De Lange, R. Schutjens, T. Debelhoir, J. Groen, D. Szombati, D. Thoen, T. Klapwijk, R. Hanson, and L. DiCarlo, Probing Dynamics of an Electron-Spin Ensemble via a Superconducting Resonator, Phys. Rev. Lett. **110**, 067004 (2013).

[10] Z.-L. Xiang, X.-Y. Lü, T.-F. Li, J. Q. You, and F. Nori, Hybrid quantum circuit consisting of a superconducting

flux qubit coupled to a spin ensemble and a transmission-line resonator, Phys. Rev. B **87,** 144516 (2013).

[11] Y. Kubo, C. Grezes, A. Dewes, T. Umeda, J. Isoya, H. Sumiya, N. Morishita, H. Abe, S. Onoda, T. Ohshima, *et al.*, Hybrid Quantum Circuit With a Superconducting Qubit Coupled to a Spin Ensemble, Phys. Rev. Lett. **107,** 220501 (2011).

[12] X. Zhu, S. Saito, A. Kemp, K. Kakuyanagi, S.-i. Karimoto, H. Nakano, W. J. Munro, Y. Tokura, M. S. Everitt, K. Nemoto, *et al.*, Coherent coupling of a superconducting flux qubit to an electron spin ensemble in diamond, Nature **478,** 221 (2011).

[13] A. J. Sigillito, H. Malissa, A. M. Tyryshkin, H. Riemann, N. V. Abrosimov, P. Becker, H.-J. Pohl, M. L. Thewalt, K. M. Itoh, J. J. Morton, *et al.*, Fast, low-power manipulation of spin ensembles in superconducting microresonators, Appl. Phys. Lett. **104,** 222407 (2014).

[14] C. Grezes, Y. Kubo, B. Julsgaard, T. Umeda, J. Isoya, H. Sumiya, H. Abe, S. Onoda, T. Ohshima, K. Nakamura, *et al.*, Towards a spin-ensemble quantum memory for superconducting qubits, C. R. Phys. **17,** 693 (2016).

[15] G. Dold, C. W. Zollitsch, J. O'sullivan, S. Welinski, A. Ferrier, P. Goldner, S. de Graaf, T. Lindström, and J. J. Morton, High-Cooperativity Coupling of a Rare-Earth Spin Ensemble to a Superconducting Resonator Using Yttrium Orthosilicate as a Substrate, Phys. Rev. Appl. **11,** 054082 (2019).

[16] S. G. Carter, O. O. Soykal, P. Dev, S. E. Economou, and E. R. Glaser, Spin coherence and echo modulation of the silicon vacancy in $4h - SiC$ at room temperature, Phys. Rev. B **92,** 161202 (2015).

[17] P. Rabl, P. Cappellaro, M. G. Dutt, L. Jiang, J. Maze, and M. D. Lukin, Strong magnetic coupling between an electronic spin qubit and a mechanical resonator, Phys. Rev. B **79,** 041302 (2009).

[18] A. Angerer, K. Streltsov, T. Astner, S. Putz, H. Sumiya, S. Onoda, J. Isoya, W. J. Munro, K. Nemoto, J. Schmiedmayer, *et al.*, Superradiant emission from colour centres in diamond, Nat. Phys. **14,** 1168 (2018).

[19] M. J. A. Schuetz, E. M. Kessler, G. Giedke, L. M. K. Vandersypen, M. D. Lukin, and J. I. Cirac, Universal Quantum Transducers Based on Surface Acoustic Waves, Phys. Rev. X **5,** 031031 (2015).

[20] T. Neuman, M. Eichenfield, M. Trusheim, L. Hackett, P. Narang, and D. Englund, A phononic bus for coherent interfaces between a superconducting quantum processor, spin memory, and photonic quantum networks, arXiv:2003.08383 (2020).

[21] S. Maity, L. Shao, S. Bogdanović, S. Meesala, Y.-I. Sohn, N. Sinclair, B. Pingault, M. Chalupnik, C. Chia, L. Zheng, *et al.*, Coherent acoustic control of a single silicon vacancy spin in diamond, Nat. Commun. **11,** 1 (2020).

[22] A. D. O'Connell, M. Hofheinz, M. Ansmann, R. C. Bialczak, M. Lenander, E. Lucero, M. Neeley, D. Sank, H. Wang, M. Weides, *et al.*, Quantum ground state and single-phonon control of a mechanical resonator, Nature **464,** 697 (2010).

[23] P. Arrangoiz-Arriola and A. H. Safavi-Naeini, Engineering interactions between superconducting qubits and phononic nanostructures, Phys. Rev. A **94,** 063864 (2016).

[24] P. Arrangoiz-Arriola, E. A. Wollack, M. Pechal, J. D. Witmer, J. T. Hill, and A. H. Safavi-Naeini, Coupling a Superconducting Quantum Circuit to a Phononic Crystal Defect Cavity, Phys. Rev. X **8,** 031007 (2018).

[25] K. J. Satzinger, Y. Zhong, H.-S. Chang, G. A. Peairs, A. Bienfait, M.-H. Chou, A. Cleland, C. R. Conner, É. Dumur, J. Grebel, *et al.*, Quantum control of surface acoustic-wave phonons, Nature **563,** 661 (2018).

[26] P. Arrangoiz-Arriola, A. Wollack, M. Pechal, Z. Wang, W. Jiang, T. McKenna, and A. Safavi-Naeini, in *APS March Meeting Abstracts* (American Physical Society, Boston, Massachusetts, 2019), Vol. 2019, p. S29–011.

[27] A. Bienfait, K. J. Satzinger, Y. Zhong, H.-S. Chang, M.-H. Chou, C. R. Conner, É. Dumur, J. Grebel, G. A. Peairs, R. G. Povey, *et al.*, Phonon-mediated quantum state transfer and remote qubit entanglement, Science **364,** 368 (2019).

[28] G. Peterson, S. Kotler, F. Lecocq, K. Cicak, X. Jin, R. Simmonds, J. Aumentado, and J. Teufel, Ultrastrong Parametric Coupling between a Superconducting Cavity and a Mechanical Resonator, Phys. Rev. Lett. **123,** 247701 (2019).

[29] M. C. Kuzyk and H. Wang, Scaling Phononic Quantum Networks of Solid-State Spins with Closed Mechanical Subsystems, Phys. Rev. X **8,** 041027 (2018).

[30] X. Li, M. C. Kuzyk, and H. Wang, Honeycomblike Phononic Networks of Spins with Closed Mechanical Subsystems, Phys. Rev. Appl. **11,** 064037 (2019).

[31] H. Wang and I. Lekavicius, Coupling spins to nanomechanical resonators: Toward quantum spin-mechanics, Appl. Phys. Lett. **117,** 230501 (2020).

[32] P. Rabl, S. J. Kolkowitz, F. Koppens, J. Harris, P. Zoller, and M. D. Lukin, A quantum spin transducer based on nanoelectromechanical resonator arrays, Nat. Phys. **6,** 602 (2010).

[33] I. Lekavicius, T. Oo, and H. Wang, Diamond Lamb wave spin-mechanical resonators with optically coherent nitrogen vacancy centers, J. Appl. Phys. **126,** 214301 (2019).

[34] G. Joe, C. Chia, M. Chalupnik, B. Pingault, S. Meesala, E. Cornell, D. Assumpcao, B. Machielse, and M. Lončar, in *CLEO: QELS_Fundamental Science* (Optical Society of America, San Jose, California, 2021), p. FTh4M–1.

[35] H. Raniwala, S. Krastanov, M. Eichenfield, and D. Englund, A spin-optomechanical quantum interface enabled by an ultrasmall mechanical and optical mode volume cavity, arXiv:2202.06999 (2022).

[36] J. Teissier, A. Barfuss, P. Appel, E. Neu, and P. Maletinsky, Strain Coupling of a Nitrogen-Vacancy Center Spin to a Diamond Mechanical Oscillator, Phys. Rev. Lett. **113,** 020503 (2014).

[37] A. Barfuss, J. Teissier, E. Neu, A. Nunnenkamp, and P. Maletinsky, Strong mechanical driving of a single electron spin, Nat. Phys. **11,** 820 (2015).

[38] M. Kjaergaard, M. E. Schwartz, J. Braumüller, P. Krantz, J. I.-J. Wang, S. Gustavsson, and W. D. Oliver, Superconducting qubits: Current state of play, Annu. Rev. Condens. Matter Phys. **11,** 369 (2020).

[39] M. H. Devoret and R. J. Schoelkopf, Superconducting circuits for quantum information: an outlook, Science **339,** 1169 (2013).

[40] C. Hepp, T. Müller, V. Waselowski, J. N. Becker, B. Pingault, H. Sternschulte, D. Steinmüller-Nethl, A. Gali, J. R. Maze, M. Atatüre, *et al.*, Electronic Structure of the Silicon Vacancy Color Center in Diamond, Phys. Rev. Lett. **112,** 036405 (2014).

[41] S. Meesala, Y.-I. Sohn, B. Pingault, L. Shao, H. A. Atikian, J. Holzgrafe, M. Gündoğan, C. Stavrakas, A. Sipahigil, C. Chia, *et al.*, Strain engineering of the silicon-vacancy center in diamond, Phys. Rev. B **97,** 205444 (2018).

[42] P. Krantz, M. Kjaergaard, F. Yan, T. P. Orlando, S. Gustavsson, and W. D. Oliver, A quantum engineer's guide to superconducting qubits, Appl. Phys. Rev. **6,** 021318 (2019).

[43] M. Mirhosseini, A. Sipahigil, M. Kalaee, and O. Painter, Superconducting qubit to optical photon transduction, Nature **588,** 599 (2020).

[44] C.-L. Zou, X. Han, L. Jiang, and H. X. Tang, Cavity piezomechanical strong coupling and frequency conversion on an aluminum nitride chip, Phys. Rev. A **94,** 013812 (2016).

[45] S. Meesala, Y.-I. Sohn, H. A. Atikian, S. Kim, M. J. Burek, J. T. Choy, and M. Lončar, Enhanced Strain Coupling of Nitrogen-Vacancy Spins to Nanoscale Diamond Cantilevers, Phys. Rev. Appl. **5,** 034010 (2016).

[46] A. J. Keller, P. B. Dieterle, M. Fang, B. Berger, J. M. Fink, and O. Painter, Al transmon qubits on silicon-on-insulator for quantum device integration, Appl. Phys. Lett. **111,** 042603 (2017).

[47] A. J. Keller, P. B. Dieterle, M. Fang, B. Berger, J. M. Fink, and O. Painter, Superconducting qubits on silicon substrates for quantum device integration, arXiv:1703.10195 (2017).

[48] K. Saito, in *Proceedings of the 10th International Conference on RF Superconductivity, Tsukuba, Japan* (High Energy Accelerator Research Organization, Tsukuba, Japan, 2001).

[49] H. R. Kerchner, D. K. Christen, and S. T. Sekula, Critical fields $H_c$ and $H_{c2}$ of superconducting niobium, Phys. Rev. B **24,** 1200 (1981).

[50] D. K. Finnemore, T. F. Stromberg, and C. A. Swenson, Superconducting properties of high-purity niobium, Phys. Rev. **149,** 231 (1966).

[51] H. Löbl, M. Klee, R. Milsom, R. Dekker, C. Metzmacher, W. Brand, and P. Lok, Materials for bulk acoustic wave (BAW) resonators and filters, J. Eur. Ceram. Soc. **21,** 2633 (2001).

[52] H. Loebl, M. Klee, C. Metzmacher, W. Brand, R. Milsom, and P. Lok, Piezoelectric thin AlN films for bulk acoustic wave (BAW) resonators, Mater. Chem. Phys. **79,** 143 (2003).

[53] D. A. Golter and H. Wang, Optically Driven Rabi Oscillations and Adiabatic Passage of Single Electron Spins in Diamond, Phys. Rev. Lett. **112,** 116403 (2014).

[54] D. A. Golter, T. Oo, M. Amezcua, I. Lekavicius, K. A. Stewart, and H. Wang, Coupling a Surface Acoustic Wave to an Electron Spin in Diamond via a Dark State, Phys. Rev. X **6,** 041060 (2016).

[55] D. A. Golter, T. Oo, M. Amezcua, K. A. Stewart, and H. Wang, Optomechanical Quantum Control of a Nitrogen-Vacancy Center in Diamond, Phys. Rev. Lett. **116,** 143602 (2016).

[56] M. Akiyama, K. Kano, and A. Teshigahara, Influence of growth temperature and scandium concentration on piezoelectric response of scandium aluminum nitride alloy thin films, Appl. Phys. Lett. **95,** 162107 (2009).

[57] N. Kurz, A. Ding, D. F. Urban, Y. Lu, L. Kirste, N. M. Feil, A. Žukauskaitė, and O. Ambacher, Experimental determination of the electro-acoustic properties of thin film AlScN using surface acoustic wave resonators, J. Appl. Phys. **126,** 075106 (2019).

[58] J. Bjurström, I. Katardjiev, and V. Yantchev, Lateral-field-excited thin-film Lamb wave resonator, Appl. Phys. Lett. **86,** 154103 (2005).

[59] C.-M. Lin, T.-T. Yen, Y.-J. Lai, V. V. Felmetsger, M. A. Hopcroft, J. H. Kuypers, and A. P. Pisano, Temperature-compensated aluminum nitride lamb wave resonators, IEEE Trans. Ultrason. Ferroelectr. Freq. Control **57,** 524 (2010).

[60] A. Konno, M. Sumisaka, A. Teshigahara, K. Kano, K.-y. Hashimo, H. Hirano, M. Esashi, M. Kadota, and S. Tanaka, in *2013 IEEE International Ultrasonics Symposium (IUS)* (IEEE, Prague, Czech Republic, 2013), p. 1378.

[61] M. K. Schmidt, C. G. Poulton, and M. J. Steel, Acoustic diamond resonators with ultrasmall mode volumes, Phys. Rev. Res. **2,** 033153 (2020).

[62] M. Eichenfield, J. Chan, R. M. Camacho, K. J. Vahala, and O. Painter, Optomechanical crystals, Nature **462,** 78 (2009).

[63] J. Chan, A. H. Safavi-Naeini, J. T. Hill, S. Meenehan, and O. Painter, Optimized optomechanical crystal cavity with acoustic radiation shield, Appl. Phys. Lett. **101,** 081115 (2012).

[64] M. J. Burek, J. D. Cohen, S. M. Meenehan, N. El-Sawah, C. Chia, T. Ruelle, S. Meesala, J. Rochman, H. A. Atikian, M. Markham, *et al.*, Diamond optomechanical crystals, Optica **3,** 1404 (2016).

[65] H. Ren, M. H. Matheny, G. S. MacCabe, J. Luo, H. Pfeifer, M. Mirhosseini, and O. Painter, Two-dimensional optomechanical crystal cavity with high quantum cooperativity, Nat. Commun. **11,** 1 (2020).

[66] M. A. Sillanpää, J. I. Park, and R. W. Simmonds, Coherent quantum state storage and transfer between two phase qubits via a resonant cavity, Nature **449,** 438 (2007).

[67] J. D. Strand, M. Ware, F. Beaudoin, T. A. Ohki, B. R. Johnson, A. Blais, and B. L. T. Plourde, First-order sideband transitions with flux-driven asymmetric transmon qubits, Phys. Rev. B **87,** 220505 (2013).

[68] D. C. McKay, S. Filipp, A. Mezzacapo, E. Magesan, J. M. Chow, and J. M. Gambetta, Universal Gate for Fixed-Frequency Qubits via a Tunable Bus, Phys. Rev. Appl. **6,** 064007 (2016).

[69] A. Premkumar, C. Weiland, S. Hwang, B. Jäck, A. P. Place, I. Waluyo, A. Hunt, V. Bisogni, J. Pelliciari, A. Barbour, *et al.*, Microscopic relaxation channels in materials for superconducting qubits, Commun. Mater. **2,** 1 (2021).

[70] D. D. Sukachev, A. Sipahigil, C. T. Nguyen, M. K. Bhaskar, R. E. Evans, F. Jelezko, and M. D. Lukin, Silicon-Vacancy Spin Qubit in Diamond: A Quantum Memory Exceeding 10 ms with Single-Shot State Readout, Phys. Rev. Lett. **119,** 223602 (2017).

[71] B. Pingault, D.-D. Jarausch, C. Hepp, L. Klintberg, J. N. Becker, M. Markham, C. Becher, and M. Atatüre, Coherent control of the silicon-vacancy spin in diamond, Nat. Commun. **8,** 1 (2017).

[72] M. H. Metsch, K. Senkalla, B. Tratzmiller, J. Scheuer, M. Kern, J. Achard, A. Tallaire, M. B. Plenio, P. Siyushev, and F. Jelezko, Initialization and Readout of Nuclear Spins via a Negatively Charged Silicon-Vacancy Center in Diamond, Phys. Rev. Lett. **122,** 190503 (2019).

[73] S. Maity, B. Pingault, G. Joe, M. Chalupnik, D. Assumpção, E. Cornell, L. Shao, and M. Lončar, Coherent coupling of mechanics to a single nuclear spin, arXiv:2107.10961 (2021).

[74] A. Akhiezer, On the absorption of sound in solids, Journal of Physics (Moscow) **1,** 277 (1939).

[75] K. Kunal and N. Aluru, Akhiezer damping in nanostructures, Phys. Rev. B **84,** 245450 (2011).

[76] J. Chan, California Institute of Technology, 2012.

[77] E. A. Wollack, A. Y. Cleland, P. Arrangoiz-Arriola, T. P. McKenna, R. G. Gruenke, R. N. Patel, W. Jiang, C. J. Sarabalis, and A. H. Safavi-Naeini, Loss channels affecting lithium niobate phononic crystal resonators at cryogenic temperature, Appl. Phys. Lett. **118,** 123501 (2021).

[78] L. Fan, X. Sun, C. Xiong, C. Schuck, and H. X. Tang, Aluminum nitride piezo-acousto-photonic crystal nanocavity with high quality factors, Appl. Phys. Lett. **102,** 153507 (2013).

[79] A. Melville, G. Calusine, W. Woods, K. Serniak, E. Golden, B. M. Niedzielski, D. K. Kim, A. Sevi, J. L. Yoder, E. A. Dauler, *et al.*, Comparison of dielectric loss in titanium nitride and aluminum superconducting resonators, Appl. Phys. Lett. **117,** 124004 (2020).

[80] W. Woods, G. Calusine, A. Melville, A. Sevi, E. Golden, D. Kim, D. Rosenberg, J. Yoder, and W. Oliver, Determining Interface Dielectric Losses in Superconducting Coplanar-Waveguide Resonators, Phys. Rev. Appl. **12,** 014012 (2019).

[81] C. R. H. McRae, H. Wang, J. Gao, M. R. Vissers, T. Brecht, A. Dunsworth, D. P. Pappas, and J. Mutus, Materials loss measurements using superconducting microwave resonators, Rev. Sci. Instrum. **91,** 091101 (2020).

[82] A. Kitaev, Fault-tolerant quantum computation by anyons, Ann. Phys. **303,** 2 (2003).

[83] R. Raussendorf, J. Harrington, and K. Goyal, Topological fault-tolerance in cluster state quantum computation, New J. Phys. **9,** 199 (2007).

[84] D. S. Wang, A. G. Fowler, A. M. Stephens, and L. C. L. Hollenberg, Threshold error rates for the toric and surface codes, arXiv:0905.0531 [quant-ph] (2009).

[85] C. Brown, A. S. Morris, A. I. Kingon, and J. Krim, Cryogenic performance of RF MEMS switch contacts, J. Microelectromech. Syst. **17,** 1460 (2008).

[86] M. Dong, G. Clark, A. J. Leenheer, M. Zimmermann, D. Dominguez, A. J. Menssen, D. Heim, G. Gilbert, D. Englund, and M. Eichenfield, High-speed programmable photonic circuits in a cryogenically compatible, visible-near-infrared 200 mm CMOS architecture, Nat. Photon. **16,** 59 (2022).

[87] N. Kalb, A. A. Reiserer, P. C. Humphreys, J. J. Bakermans, S. J. Kamerling, N. H. Nickerson, S. C. Benjamin, D. J. Twitchen, M. Markham, and R. Hanson, Entanglement distillation between solid-state quantum network nodes, Science **356,** 928 (2017).

[88] H. Bernien, B. Hensen, W. Pfaff, G. Koolstra, M. S. Blok, L. Robledo, T. Taminiau, M. Markham, D. J. Twitchen, L. Childress, *et al.*, Heralded entanglement between solid-state qubits separated by three metres, Nature **497,** 86 (2013).